XMM–Newton observations of PSR J0554+3107: pulsing thermal emission from a cooling high-mass neutron star

A. S. Tanashkin,[*] A. V. Karpova [ID], A. Y. Potekhin [ID], Y. A. Shibanov and D. A. Zyuzin [ID]

Ioffe Institute, Politekhnicheskaya 26, St Petersburg 194021, Russia

ABSTRACT

XMM–Newton observations of the middle-aged radio-quiet γ-ray pulsar J0554+3107 allowed us, for the first time, firmly identify it in X-rays by detection of pulsations with the pulsar period. In the 0.2–2 keV band, the pulse profile shows two peaks separated by about a half of the rotation phase with the pulsed fraction of 25 ± 6 per cent. The profile and spectrum in this band can be mainly described by thermal emission from the neutron star with the hydrogen atmosphere, dipole magnetic field of $\sim 10^{13}$ G, and non-uniform surface temperature. Non-thermal emission from the pulsar magnetosphere is marginally detected at higher photon energies. The spectral fit with the atmosphere+power-law model implies that J0554+3107 is a rather heavy and cool neutron star with the mass of 1.6–2.1 $M_{\odot}$, the radius of ≈ 13 km, and the redshifted effective temperature of ≈ 50 eV. The spectrum shows an absorption line of unknown nature at ≈ 350 eV. Given the extinction–distance relation, the pulsar is located at ≈ 2 kpc and has the redshifted bolometric thermal luminosity of $\approx 2 \times 10^{32}$ erg s^{-1}. We discuss cooling scenarios for J0554+3107 considering plausible equations of state of superdense matter inside the star, different compositions of the heat-blanketing envelope, and various ages.

Key words: stars: neutron – pulsars: general – pulsars: individual: PSR J0554+3107.

1 INTRODUCTION

Studies of thermal emission from neutron stars (NSs) are one of the ways to investigate the properties of superdense nuclear matter in their interiors (e.g. Yakovlev & Pethick 2004). If thermal emission originates from the entire NS surface, the comparison of the measured thermal luminosity (or, equivalently, mean effective temperature) with predictions of NS cooling theories can set constraints on the equation of state (EoS) of such matter. Middle-aged (10^4–10^6 yr old) stars are the best targets for such analysis since thermal components usually dominate over non-thermal ones in their X-ray spectra. However, effective temperatures and ages are estimated only for a few dozens of NSs, which is not enough to make definite conclusions (Potekhin et al. 2020).

The middle-aged radio-quiet PSR J0554+3107 (hereafter J0554) was discovered by Einstein@Home[1] in a blind search of *Fermi* Large Area Telescope (LAT) γ-ray data (Pletsch et al. 2013). Its parameters are presented in Table 1. Upper limits on the integral flux density at 111, 150, and 1400 MHz are 0.5, 1.2, and 0.066 mJy, respectively (Pletsch et al. 2013; Grießmeier et al. 2021; Tyul'bashev, Kitaeva & Tyulbasheva 2021).

The pulsar is projected on to the supernova remnant (SNR) G179.0+2.6 and likely associated with it (Pletsch et al. 2013). This is a shell-type oxygen-rich remnant (How et al. 2018) with the diameter of about 70 arcmin. Its age is unclear: the large diameter and the low surface brightness imply the age of $\sim$10–100 kyr, but

the radial configuration of the magnetic field is typical for young SNRs (Fuerst & Reich 1986; Gao et al. 2011). There are different estimates of the distance to the remnant, from about 3 to 6 kpc (Case & Bhattacharya 1998; Guseinov et al. 2003; Pavlovic et al. 2014), obtained through empirical correlations between the radio surface brightness and the diameter of the SNR. However, recent studies show that G179.0+2.6 can be much closer, at $\approx$0.9 kpc (Zhao et al. 2020). This result is based on an apparent interstellar extinction jump at this distance along the remnant line of sight and on the assumption that it is associated with the dust formed by the SNR. However, the detected extinction jump may correspond to a foreground molecular cloud and not the remnant itself. If so, this value should be considered as the lower limit to the distance.

Since J0554 has not been detected in radio, it is not possible to obtain the distance basing on the dispersion measure. The only available estimate is the so-called 'pseudo-distance' of $\approx$1.9 kpc calculated from the empirical relation between the distance and the pulsar γ-ray flux (Saz Parkinson et al. 2010). Though such an estimate is rather uncertain (within a factor of 2–3), it is consistent with the association of J0554 with G179.0+2.6.

Zyuzin, Karpova & Shibanov (2018) found the likely X-ray counterpart of J0554 in the 1st *Swift*-XRT Point Source (1SXPS) catalogue (Evans et al. 2014). 17 counts were detected from the source in the 11 ks exposure, and 13 of them are in the 0.3–1 keV band, which indicates that the source is soft. Indeed, fitting the X-ray spectrum with a power-law model, Zyuzin et al. (2018) obtained the photon index $\Gamma > 4$, which is too high for pulsars and may indicate the presence of a thermal-like spectral component. Pure thermal emission models – the blackbody and the NS atmosphere – resulted in NS surface temperatures of $\approx$50–100 eV. In any case, the obtained

Table 1. J0554 parameters obtained from Pletsch et al. (2013). Numbers in parentheses denote 1σ uncertainties relating to the last significant digit quoted.

RA (J2000)	$05^{\rm h}54^{\rm m}05\overset{\rm s}{.}01(3)$
Dec. (J2000)	$+31°07'41''(4)$
Galactic longitude l (°)	179.058
Galactic latitude b (°)	2.697
Spin period P (ms)	465
Spin frequency f (Hz)	2.15071817570(7)
Frequency derivative $\dot{f}$ (Hz s^{-1})	$-0.659622(5) \times 10^{-12}$
Frequency second derivative $\ddot{f}$ (Hz s^{-2})	$0.18(2) \times 10^{-23}$
Epoch of frequency determination (MJD)	55214
Data time span (MJD)	54702–56383
Solar system ephemeris model	DE405
Characteristic age $t_{\rm c}$ (kyr)	51.7
Spin-down luminosity $\dot{E}$ (erg s^{-1})	5.6×10^{34}
Characteristic magnetic field $B_{\rm c}$ (G)	8.2×10^{12}

model parameters remained very uncertain because of the low *Swift* count statistics. We therefore performed deeper observations with *XMM–Newton* to confirm the counterpart of J0554 and clarify its X-ray properties.

Here we present results of these observations. The data and the reduction procedure are presented in Section 2. Imaging is described in Section 3. Timing and spectral analyses are presented correspondingly in Section 4 and Section 5. We discuss the results in Section 6 and make conclusions in Section 7.

2 OBSERVATIONS AND DATA REDUCTION

45-ks *XMM–Newton* observations of the J0554 field were carried out on 2021 October 7 (ObsID 0883760101, PI: A. Karpova). The European Photon Imaging Camera-Metal Oxide Semiconductor (EPIC-MOS) detectors were operated in the full frame mode and the EPIC-pn (PN hereafter) detector in the large window mode. The corresponding imaging areas are 28×28 arcmin^2 and 13.5×26 arcmin^2. For all instruments, the thin filter was chosen.

We used the *XMM–Newton* Science Analysis Software (XMM-SAS) v.19.1.0 for analysis. The EMPROC and EPPROC routines were utilized to reprocess the data. To filter out the periods of background flares, we extracted high-energy light curves from the fields of view (FoVs) of all EPIC detectors. Only one short flare is present (see Fig. 1), mostly affecting the PN detector, but also having a slight impact on the MOS1 light curve, so we cleaned only the PN and MOS1 data, leaving the MOS2 data unfiltered. As a result, the effective exposures are 44.3, 44.5, and 38.8 ks for MOS1, MOS2, and PN cameras, respectively. Single, double, triple, and quadruple pixel events were selected for MOS (PATTERN $\leq$ 12) and single and double pixel events for PN (PATTERN $\leq$ 4).

3 IMAGING

Using the 'images' script[2] (Willatt & Ehle 2016), we created combined MOS+PN exposure-corrected images in different energy bands. The resulting image is shown in Fig. 2. The J0554 candidate counterpart is seen as a bright source in the centre. Its position RA = $05^{\rm h}54^{\rm m}05\overset{\rm s}{.}067(10)$ and Dec. = $+31°07'41''.40(13)$ was derived by the EDETECT_CHAIN task using the data from all EPIC detectors
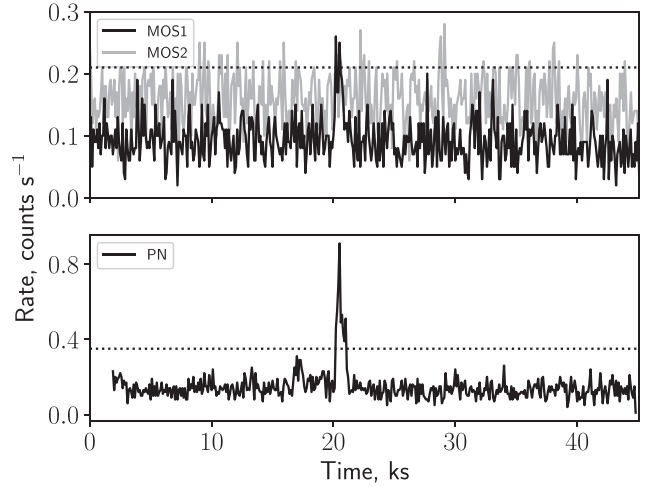
Figure 1. High-energy light curves extracted from the FoVs of the MOS (>10 keV; top) and PN (10–12 keV; bottom) cameras. The dotted lines show the thresholds applied to filter the MOS1 and PN data for periods of background flaring activity (no filtering was applied to the MOS2 data).
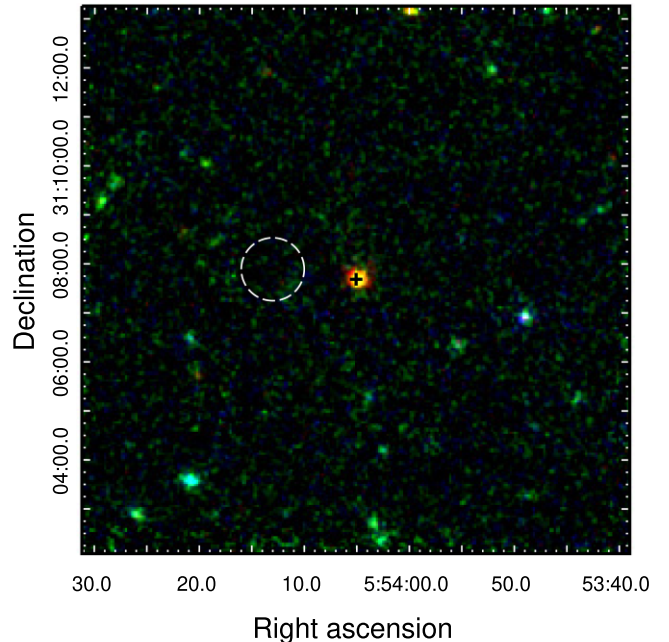

Figure 2. *XMM–Newton* combined (MOS1+MOS2+PN) image of the J0554 field obtained in soft (0.2–1 keV, red), medium (1–2 keV, green), and hard (2–12 keV, blue) energy bands. The bright soft point source in the centre of the image is the X-ray counterpart of the pulsar, whose γ-ray position is marked by the cross. The position uncertainty is significantly smaller than the marker size and is not shown. The dashed 38.5-arcsec radius circle shows the region used for the background extraction in the timing and spectral analyses.

(numbers in parentheses are 1σ pure statistical uncertainties). Taking into account the *XMM–Newton* absolute pointing accuracy of 1.2 arcsec,[3] the coordinates are in agreement within 1σ with the J0554 ones obtained from the *Fermi* data (Table 1).

From Fig. 2 one can see that the J0554 candidate counterpart is a soft source. No extended emission like a pulsar wind nebula (PWN)
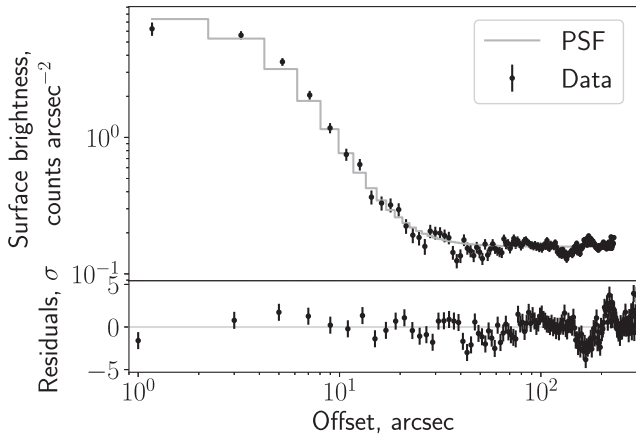
Figure 3. Comparison of the *XMM–Newton* PSF and the observed radial brightness profile obtained from the PN data in the 0.2–10 keV energy band.

or misaligned outflows are seen in the pulsar vicinity. However, the *XMM–Newton* point spread function (PSF) is rather wide and the compact PWN if exists can be blurred with the pulsar. To treat this possibility more carefully we used the ERADIAL tool, which extracts the source radial brightness profile and fits the PSF to it. The result is shown in Fig. 3, and we can conclude that the radial profile is consistent with the PSF and no compact PWN is resolved. We also do not resolve any extended emission in the *XMM–Newton* FoV that could be identified with the SNR G179.0+2.6, whose radio shell is outside the FoV.

4 TIMING ANALYSIS

The PN detector operating in the large window mode provides the time resolution of $\approx$48 ms, which is sufficient to search for regular X-ray pulsations with the 465 ms spin period of J0554. We used the BARYCEN task and DE405 ephemeris to apply the barycentric correction and then extracted filtered for background flaring activity events in the 0.2–2 keV band from the 22-arcsec radius circle aperture centred at the pulsar position. The aperture was selected using the EREGIONANALYSE task that produces the optimum extraction radius basing on signal-to-noise ratio. This results in 1026 source counts or $\approx$98 per cent of the total number of source counts detected in the whole PN energy band. To search for the pulsations, we performed the Z_n^2-test (Buccheri et al. 1983) for the number of harmonics n from 1 to 5 using the 0.8 mHz window around the spin frequency of 2.150474376(14) Hz expected at the epoch of the *XMM–Newton* observation (MJD 59494) according to the *Fermi* timing results (Table 1). We detected pulsations at the frequency of 2.150493(2) Hz and found statistically significant contributions from two leading harmonics. The resulting periodogram is shown in Fig. 4. The maximum $Z_2^2 = 42.7$, which implies the detection confidence level of $\approx$4.7σ.[4]

We note that the frequency detected in X-rays is somewhat higher than the predicted one. This can be due to the pulsar timing noise and/or glitches, which might have occurred during the $\sim$8 yr period between the last γ-ray observations of 2013, included by Pletsch et al. (2013) into the *Fermi* timing solution, and the *XMM–Newton* observations of 2021. For instance, the relative difference $\log(\Delta f/f) \approx -5.1$ is consistent with the distribution of
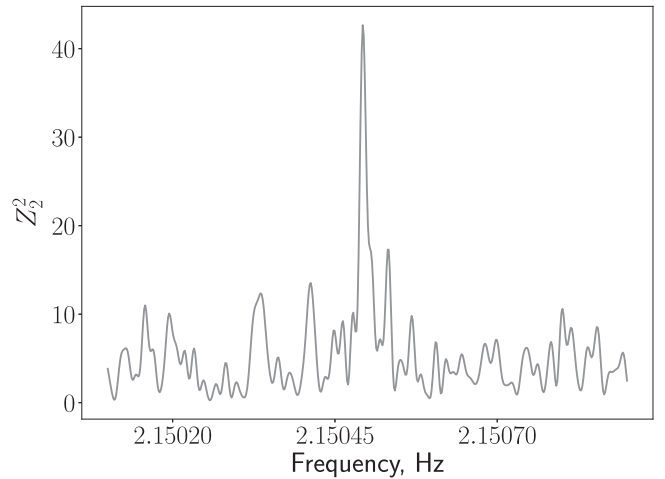
<hr>

[4]See Appendix A for details.

Figure 4. Z_2^2-test periodogram for J0554 in the 0.2–2 keV energy band.
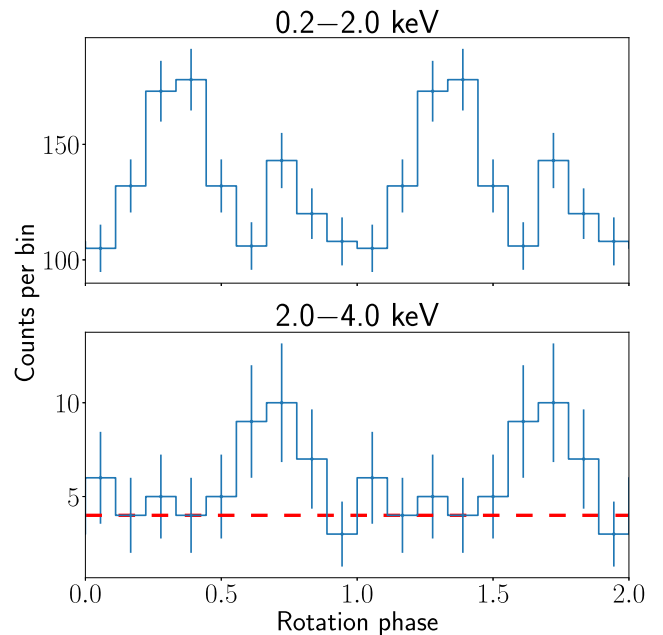

Figure 5. Pulse profiles of J0554 in the 0.2–2 keV and 2–4 keV energy bands. Two phase cycles are plotted for clarity. The dashed red line in the bottom panel indicates the background level. In the 0.2–2 keV band the background level ($\approx$19 counts per bin) is significantly below the minimum of the pulse profile and the bottom boundary of the plot.

the relative glitch sizes $\log(\Delta f_g/f)$ observed for pulsars (Lower et al. 2021).

Folded X-ray pulse profile in the 0.2–2 keV energy band is presented in the upper panel of Fig. 5. Following the approach suggested by Becker & Trümper (1999) we calculated the optimal number of phase bins to be 11. However, this value exceeds the maximum of 9 bins set by the time resolution of the PN camera and the pulsar period, so we used the latter value to construct the folded light curve. Two peaks separated by about a half of the pulsar rotation phase are clearly resolved. The pulsed fraction (PF) of the emission was calculated from the photon phases using the bootstrap method outlined in Swanepoel, de Beer & Loots (1996). The result obtained with this technique is not affected by binning effects, which is particularly important in our case since the number of counts is

low and the phase bins are wide. The resulted background-corrected PF in the 0.2–2 keV band is 25 ± 6 per cent. In the lower panel of Fig. 5, we also show the pulse profile in the 2–4 keV energy band. The pulsar possibly demonstrates single-peaked pulsations, but the count statistics in this band is too low to make definite conclusions.

5 SPECTRAL ANALYSIS

We extracted the pulsar spectra from the 19-arcsec radius aperture using EVSELECT task. This radius was chosen using the EREGION-ANALYSE task as the optimum value in terms of signal-to-noise ratio for the 0.2–10 keV band. The redistribution matrix and the ancillary response files were generated by RMFGEN and ARFGEN tools. For the background, we chose the 38.5-arcsec radius circular source-free region, located at the same CCD chip and approximately the same CCD RAWY pixel position as the source (see Fig. 2), in accordance with general recommendations by the EPIC Consortium.[5] As a result, we obtained 221, 246, and 1001 net counts in the 0.2–10 keV band from the MOS1, MOS2, and PN data, respectively. We fitted the spectra simultaneously with the X-Ray Spectral Fitting Package (XSPEC) v.12.11.1 (Arnaud 1996) using the TBABS model with the WILM abundances (Wilms, Allen & McCray 2000) to take into account the interstellar medium (ISM) absorption.

At first, we grouped the spectra to ensure at least 25 counts per energy bin and used χ^2-statistics to preliminarily check, which of the models, typically used to describe pulsars X-ray emission, can fit the data. The single POWERLAW (PL) model, corresponding to the NS magnetosphere emission, though statistically acceptable (χ_ν^2/degrees of freedom (dof) = 1.03/41) resulted in a photon index $\Gamma \approx 7$, which is too high to be consistent with typical slopes of non-thermal X-ray spectra of pulsars (e.g. Kargaltsev & Pavlov 2008). Addition of the blackbody (BB) component (model BBODYRAD in XSPEC) still gives a too high photon index, while the single BB model fits the spectrum worse (χ_ν^2/dof = 2.02/43). In contrast, the BB+BB model, composed of two BB components with different temperatures and radii of equivalent emitting spheres, is statistically acceptable with χ_ν^2/dof = 1.09/41. This model is usually assumed to describe thermal emission from some colder and hotter areas of the NS surface. However, there is some flux excess above the model at energies $\gtrsim$2 keV. Although its significance is low, this may indicate the presence of the non-thermal emission. Thus, we added the PL component to the BB+BB model, which resulted in χ_ν^2/dof = 1.04/39 and a reasonable photon index $\Gamma \lesssim 3$.

We also constructed the hydrogen atmosphere models NSMDINTB for the NS with a dipole magnetic field to fit the thermal spectral component. In these models, which are described in Appendix B, free parameters are: the NS mass M and radius R, the distance D, the angle α between the axis of rotation and the magnetic axis, the angle ζ between the rotation axis and the line of sight, and the redshifted effective temperature $T^\infty = T/(1 + z_g)$, where z_g is the gravitational redshift at the NS surface. The effective surface temperature T is defined by the total thermal luminosity L according to the relation $L \equiv 4\pi\sigma_{SB}R^2T^4$, where σ_{SB} is the Stefan–Boltzmann constant. We used two values of the magnetic field at the pole close to the estimates based on the dipole spin-down formula (see Appendix B), $B_p = 10^{13}$ and 2×10^{13} G (hereafter NS130 and NS133, respectively). We obtained rather poor fits with χ_ν^2/dof = 1.60/39 for NS130 and χ_ν^2/dof = 1.55/39 for NS133. However, we found that addition of
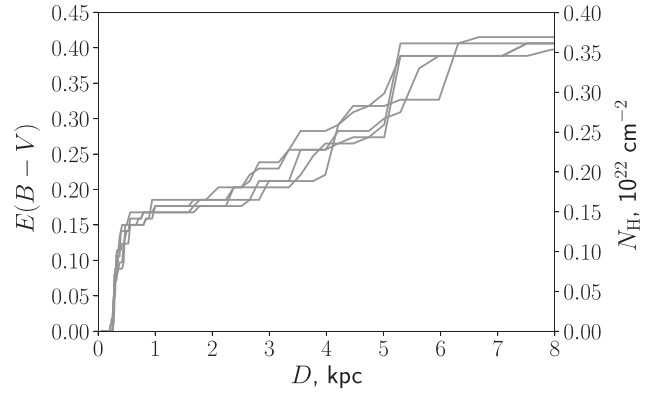
[5]See e.g. Footnote 3, pages 28–29.

Figure 6. Interstellar extinction–distance relation in the J0554 direction obtained from the dust map of Green et al. (2019).

an absorption Gaussian line (model GABS in XSPEC) at ≈0.35 keV significantly improves the fit resulting in χ_ν^2/dof = 1.15/36 and 1.17/36. Addition of the PL component to describe the flux excess at high energies slightly improves the fits leading to χ_ν^2/dof = 1.15/34 and 1.07/34. Basing on these preliminary tests, we further focused on the models 2BB+PL and (NSMDINTB + PL) × GABS as the ones providing the best-fitting statistics.

The number of collected source counts is not large and for more rigorous analysis we regrouped the spectra to ensure at least 1 count per energy bin. This allows us to obtain the most robust estimates of the J0554 spectral parameters. We applied *W*-statistics (Wachter, Leach & Kellogg 1979) appropriate for Poisson data with Poisson background[6] and performed the fitting using the Markov chain Monte Carlo (MCMC) technique. We utilized the Bayesian parameter estimation procedure using PYXSPEC interface and the PYTHON package EMCEE (Foreman-Mackey et al. 2013), which implements the affine-invariant MCMC sampler developed by Goodman & Weare (2010). The best-fitting model parameters, defined as the ones corresponding to the maximum values of probability density, were derived from the sampled posterior distributions together with their 1σ credible intervals.

The Bayesian inference also allows us to include some additional information in the fitting procedure. We used the 3D map[7] of the dust distribution in the Galaxy based on *Gaia*, Panoramic Survey Telescope and Rapid Response System 1 (Pan-STARRS 1), and Two Micron All Sky Survey (2MASS) data (Green et al. 2019) to obtain the extinction–distance relation in the J0554 direction. In Fig. 6, we show five representative samples of this relation drawn from the posterior distribution of the distance–reddening profiles (see Green et al. 2019 for details). The following procedure was used. At each step of the MCMC fitting, we randomly take one of the five samples and use the relation $N_H = a \times 10^{21}E(B - V)$ to convert the selective reddening $E(B - V)$ into the equivalent hydrogen column density N_H, which is responsible for the ISM absorption in X-rays. The conversion factor a is drawn from the normal distribution with the mean of 8.9 and the standard deviation of 0.4 according to the empirical relation $N_H = (2.87 \pm 0.12) \times 10^{21}A_V$ cm^{-2} (Foight et al. 2016) and implying the standard reddening law $A_V = 3.1E(B - V)$, where A_V is the optical extinction. Then we compute the distance D

[6]See https://heasarc.gsfc.nasa.gov/xanadu/xspec/manual/XSappendixStatistics.html
[7]http://argonaut.skymaps.info/

Table 2. Best-fitting parameters for different spectral models[a].

Model	2BB+PL	2BB+PL[b]	(2BB+PL) × GABS	(NS130 + PL) × GABS	(NS133 + PL) × GABS
N_H (10^{21} cm^{-2})	$3.1^{+0.2}_{-0.2}$	$5.2^{+0.4}_{-0.8}$	$2.3^{+0.5}_{-0.4}$	$1.62^{+0.08}_{-0.06}$	$1.66^{+0.08}_{-0.07}$
D (kpc)	$5.5^{+0.3}_{-0.5}$		$4.1^{+1.4}_{-1.4}$	$2.0^{+0.2}_{-0.4}$	$2.0^{+0.4}_{-0.2}$
Γ	2.0^{fixed}	2.0^{fixed}	2.0^{fixed}	$2.2^{+0.6}_{-0.4}$	$2.3^{+0.5}_{-0.4}$
K (10^{-6} photons cm^{-2} s^{-1} keV^{-1})	$2.2^{+0.6}_{-0.6}$	$1.9^{+0.6}_{-0.7}$	$2.1^{+0.6}_{-0.5}$	$1.6^{+1.3}_{-0.7}$	$2.0^{+1.5}_{-0.7}$
$\log L_X$ (erg s^{-1})	$31.27^{+0.13}_{-0.15}$	$29.62^{+0.20}_{-0.12} + \log D_{0.9}^2$	$31.08^{+0.20}_{-0.28}$	$30.21^{+0.15}_{-0.30}$	$30.27^{+0.19}_{-0.19}$
α (°)				70^{+20}_{-20}	60^{+20}_{-20}
ζ (°)				60^{+20}_{-10}	80^{+10}_{-30}
M (M$_\odot$)				$1.9^{+0.2}_{-0.2}$	$1.8^{+0.3}_{-0.2}$
R (km)				$13.5^{+1.2}_{-1.7}$	$13.0^{+1.5}_{-1.3}$
R^∞ (km)				$16.9^{+1.5}_{-1.3}$	$17.1^{+1.3}_{-1.3}$
$k_B T^\infty$ (eV)				47^{+2}_{-2}	49^{+2}_{-2}
R_{cold}^∞ (km)	19^{+1}_{-5}	$14^{+5}_{-6}\, D_{0.9}$	19^{+1}_{-5}		
R_{hot}^∞ (km)	$1.12^{+1.05}_{-0.11}$	$0.33^{+0.23}_{-0.20}\, D_{0.9}$	$1.19^{+0.87}_{-0.17}$		
$k_B T_{\text{cold}}^\infty$ (eV)	86^{+5}_{-4}	65^{+7}_{-3}	84^{+6}_{-10}		
$k_B T_{\text{hot}}^\infty$ (eV)	156^{+12}_{-25}	140^{+23}_{-17}	135^{+19}_{-13}		
$\log L^\infty$ (erg s^{-1})	$33.32^{+0.10}_{-0.19}$	$32.79^{+0.11}_{-0.39} + \log D_{0.9}^2$	$33.23^{+0.12}_{-0.61}$	$32.25^{+0.12}_{-0.11}$	$32.33^{+0.10}_{-0.10}$
E_0 (eV)			370^{+30}_{-70}	340^{+40}_{-40}	350^{+30}_{-50}
σ (eV)			24^{+18}_{-14}	25^{+13}_{-9}	24^{+14}_{-8}
τ (eV)			>40	>680	>890
EW (eV)			<430	150^{+120}_{-40}	180^{+70}_{-70}
W/dof	240/216	231/216	228/213	228/211	228/211
χ_ν^2/dof	1.46/40	1.16/40	1.14/37	1.27/34	1.27/34

[a]N_H is the absorbing column density; D is the distance; Γ is the photon index; K is the PL normalization; L_X is the non-thermal luminosity in the 2–10 keV band; α is the angle between the axis of rotation and the magnetic axis; ζ is the angle between the rotation axis and the line of sight; M is the NS mass; R and $R^\infty = R(1 + z_g)$ are the intrinsic and apparent radii of the NS; $T^\infty = T/(1 + z_g)$ is the atmosphere redshifted effective temperature; R_{cold}^∞ and R_{hot}^∞ are the apparent radii of the equivalent emitting spheres; T_{cold}^∞ and T_{hot}^∞ are the redshifted effective temperatures of the cold and hot BB components; $L^\infty = L/(1 + z_g)^2$ is the apparent bolometric thermal luminosity; E_0, σ, τ, and EW are the absorption line centre, width, depth, and equivalent width; and z_g is the gravitational redshift. All errors are at 1σ credible intervals, while the lower and upper limits are set at 98 per cent. The last two rows provide the minimum values of W-statistics, which was used as a log-likelihood in the MCMC procedure, and χ_ν^2 calculated for the spectra that were grouped to ensure at least 25 counts per bin.
[b]In this case, in contrast to all other models, the N_H–D relation was not used in the fitting procedure (see text for details). $D_{0.9} \equiv D/0.9$ kpc, where 0.9 kpc is the lower limit of the distance to J0554 obtained from its association with the SNR G179.0+2.6 (Zhao et al. 2020).

using linear interpolation between the closest sample values $\underline{N_H}$ and $\overline{N_H}$ such that $\underline{N_H} \leq N_H \leq \overline{N_H}$.

In contrast to NSMDINTB models, where both the NS radius and the distance are free parameters, the BB model has a normalization $N = (R_{\text{BB}}^\infty/D)^2$ as a free parameter, where R_{BB}^∞ is the apparent radius of the equivalent emitting sphere. Thus, in the case of the 2BB+PL model at each step we independently sampled the radii R_{cold}^∞ and R_{hot}^∞ for colder and hotter emitting areas and then calculated normalizations using these values together with the computed distance. We constrained both radii to be $\leq$20 km as a reasonable value of an NS radius measured by a distant observer.

For the (NSMDINTB + PL) × GABS models, we used a prior $\alpha + \zeta \geq 90°$, which follows from the shape of the folded light curve and the PF value. The PL photon indices Γ were constrained in the range of 0.5–3 typical for pulsars (e.g. Kargaltsev & Pavlov 2008). However, in the case of the 2BB+PL model, Γ tends to the upper bound, while the temperature of the hotter BB component in general takes slightly lower values than that in the case of the pure BB+BB model. This behaviour is typical for situations when the PL component competes with the hotter BB component at lower energies, while the number of counts above $\sim$2 keV is very low and the PL slope there is poorly constrained. This is exactly the case

of J0554. Thus, we applied the fixed photon index $\Gamma = 2$ for the 2BB+PL model.

The best-fitting parameters are presented in Table 2. The pulsar spectrum with the best-fitting model (NS133 + PL) × GABS is shown in Fig. 7. In Fig. 8, we present a corner plot of posterior distribution functions for some parameters of this model. To check the fit quality, we calculated values of the χ^2-statistics using the spectra grouped to ensure at least 25 counts per bin. They are provided in the last row of Table 2. These χ^2 values differ from the preliminary ones partially due to inclusion of parameter constraints in the fitting procedure.

The Gaussian line model GABS describing the spectral feature is represented as

$$\mathfrak{G}(E) = \exp\left(-\frac{\tau}{\sqrt{2\pi}\sigma}\, e^{-\frac{(E-E_0)^2}{2\sigma^2}}\right), \tag{1}$$

where E_0, σ, and τ are the line centre, width, and depth. τ is poorly defined from the spectral fits and we provide only its lower limits. We also calculated the line equivalent width (EW) defined as

$$\text{EW} = \int (1 - \mathfrak{G}(E))\, dE, \tag{2}$$
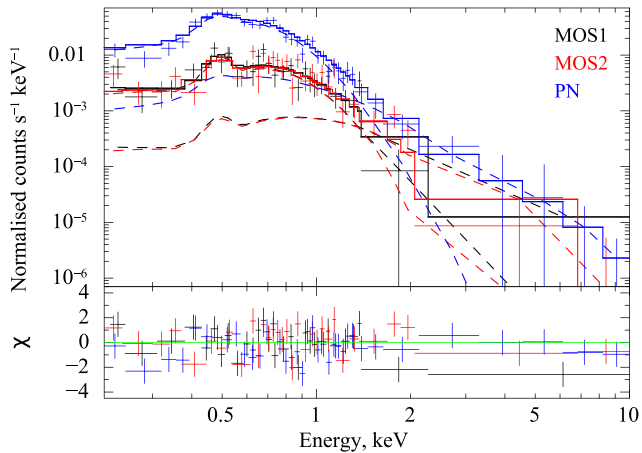
which is better constrained by the fits.

Figure 7. J0554 spectrum, best-fitting model (NS133 + PL) × GABS, and residuals. The dashed lines show the model components. Data from different detectors are shown by different colours. For illustrative purposes, spectra were regrouped using XSPEC command REBIN to reach at least 2σ detection significance in each new bin (but no more than 12 adjacent bins were allowed to be combined).

From the second column of Table 2, one can see that the 2BB+PL model fails to fit the data when the N_H–D relation is used. We have found that it describes the spectrum poorly at energies $\lesssim 0.4$ keV, where the model flux becomes systematically higher than the observed one. Exclusion of the N_H–D prior removes the discrepancy in the soft band and results in the statistically acceptable fit (the third column of Table 2). However, for reasonable BB normalizations, which imply the apparent radii of $\lesssim 20$ km and the distances of $\gtrsim 0.9$ kpc, the obtained column densities are about 1.5 times higher than the maximum value provided by the dust map of Green et al. (2019); see Fig. 6. Recalling that the addition of the Gaussian absorption line significantly improves the fit in the case of the atmosphere models, we tried to add the line to the 2BB+PL model as well. This leads to the good fit without N_H anomalies even when the N_H–D relation is implemented (see the fourth column in Table 2).

6 DISCUSSION

6.1 J0554 spectral and timing properties

The time-integrated X-ray spectrum of J0554 can be well described by the composite emission models containing the thermal and non-thermal spectral components. For the former, we tried the BB model, which imitates the emission from the solid or liquid state NS surface, and the hydrogen atmosphere models with dipole magnetic fields.

In the case of the 2BB+PL model without the N_H–D prior, we assume that the cold BB component originates from the bulk of the stellar surface, while the hot component describes emission from a hotspot (e.g. polar caps). Then the distance to J0554 should be $\lesssim 2$ kpc, otherwise the radius of the cold component will be inadequately large (see the third column of Table 2). However, the model requires a much higher column density than expected for such distance according to the dust map by Green et al. (2019). This means that either the model, being formally statistically acceptable, results in a physically inappropriate N_H and hence wrong NS parameters, or the considered N_H–D relation is incorrect in the J0554 direction. Since the pulsar is projected on to the SNR G179.0+2.6, the derived absorption excess could be provided by some filament of the remnant

even if it is not visible in X-rays. Unfortunately, there are no X-ray extragalactic objects in the pulsar field that are bright enough to make an independent estimate of the maximum absorption in the pulsar direction. However, we checked some other extinction maps by Drimmel, Cabrera-Lavers & López-Corredoira (2003), Chen et al. (2014, 2019), Sale et al. (2014), Lallement et al. (2014, 2018), and Capitanio et al. (2017). All of them provide $N_\mathrm{H} \lesssim 3.5 \times 10^{21}$ cm^{-2} at 2 kpc that is significantly smaller than the best-fitting value. Moreover, basing on the [O III]/Hα emission ratio measured for the SNR G179.0+2.6 associated with J0554, How et al. (2018) argued that $E(B - V)$ should not be much greater than 0.3 (i.e. $N_\mathrm{H} \lesssim 2.7 \times 10^{21}$ cm^{-2}). This makes the 2BB+PL model hardly acceptable without additional constraints and model components.

Implementation of the N_H–D prior along with the addition of the low energy absorption feature solves the 2BB+PL problem, resulting in about twice lower column density and acceptable fit statistics. If we assume that the cold BB component describes the emission from the bulk of the stellar surface, while the hot component corresponds to a hotspot, then the size of the latter is larger than the 'standard' polar cap of a radius of a few hundred meters, expected according to the model of Sturrock (1971). The obtained effective temperatures are in agreement with results for other NSs of similar age (Potekhin et al. 2020).

The (NSMDINTB + PL) × GABS models are also plausible. Parameters obtained for two different magnetic fields are very similar (see the last two columns of Table 2).[8] These models indicate that J0554 should be a rather heavy NS, with the mass of 1.6–2.1 M$_\odot$. Its redshifted effective temperature $T^\infty = 48 \pm 3$ eV (0.56 ± 0.3 MK), which is about twice lower than the temperature of the cold BB component from the bulk surface of the NS in the 2BB+PL model. This is a typical situation when the thermal NS component is equally well described by the BB and atmosphere models, since the latter spectra are harder (Potekhin 2014).

It is important, that all three statistically acceptable models implementing the N_H–D prior require the absorption feature at ≈ 0.35 keV regardless the local continuum shape. This supports the presence of the feature in the data. In the 2BB+PL model without the N_H–D relation, which we consider as hardly acceptable, the absence of the absorption line is compensated by the implausibly high N_H value. We note that there are only a few rotation-powered pulsars for which absorption lines have been reported: PSR J1740+1000 (Kargaltsev et al. 2012), PSR J0659+1414 (Arumugasamy et al. 2018; Zharikov et al. 2021; Schwope et al. 2022), PSR J0726−2612 (Rigoselli et al. 2019), PSR J1819−1458 (McLaughlin et al. 2007; Miller et al. 2013), and Calvera (Shevchuk, Fox & Rutledge 2009; Shibanov et al. 2016; Mereghetti et al. 2021). For none of these objects the nature of lines has been unambiguously established.

The nature of the J0554 feature is also unclear. One of possible explanations is a cyclotron absorption line. Such line position measured by a distant observer is given by

$$E_\mathrm{cyc}^\infty = 11.577\,(1 + z_\mathrm{g})^{-1} Z\, \frac{m_\mathrm{e}}{m}\, \frac{B}{10^{12}\,\mathrm{G}}\ \mathrm{keV}, \quad (3)$$

where m_e is the electron mass, Z and m are the charge number and mass of the particle that is responsible for the cyclotron absorption. Hence, the surface magnetic field is $\approx 4 \times 10^{10}$ G if the line is produced by electrons, and $\approx 7 \times 10^{13}$ G if it is produced by protons

---

[8]We also tried analogous models with other field strengths and found that a decrease of B_p to $\sim 2 \times 10^{12}$ G worsens the fitting statistics, while an increase to 5×10^{13} G does not noticeably change the results.

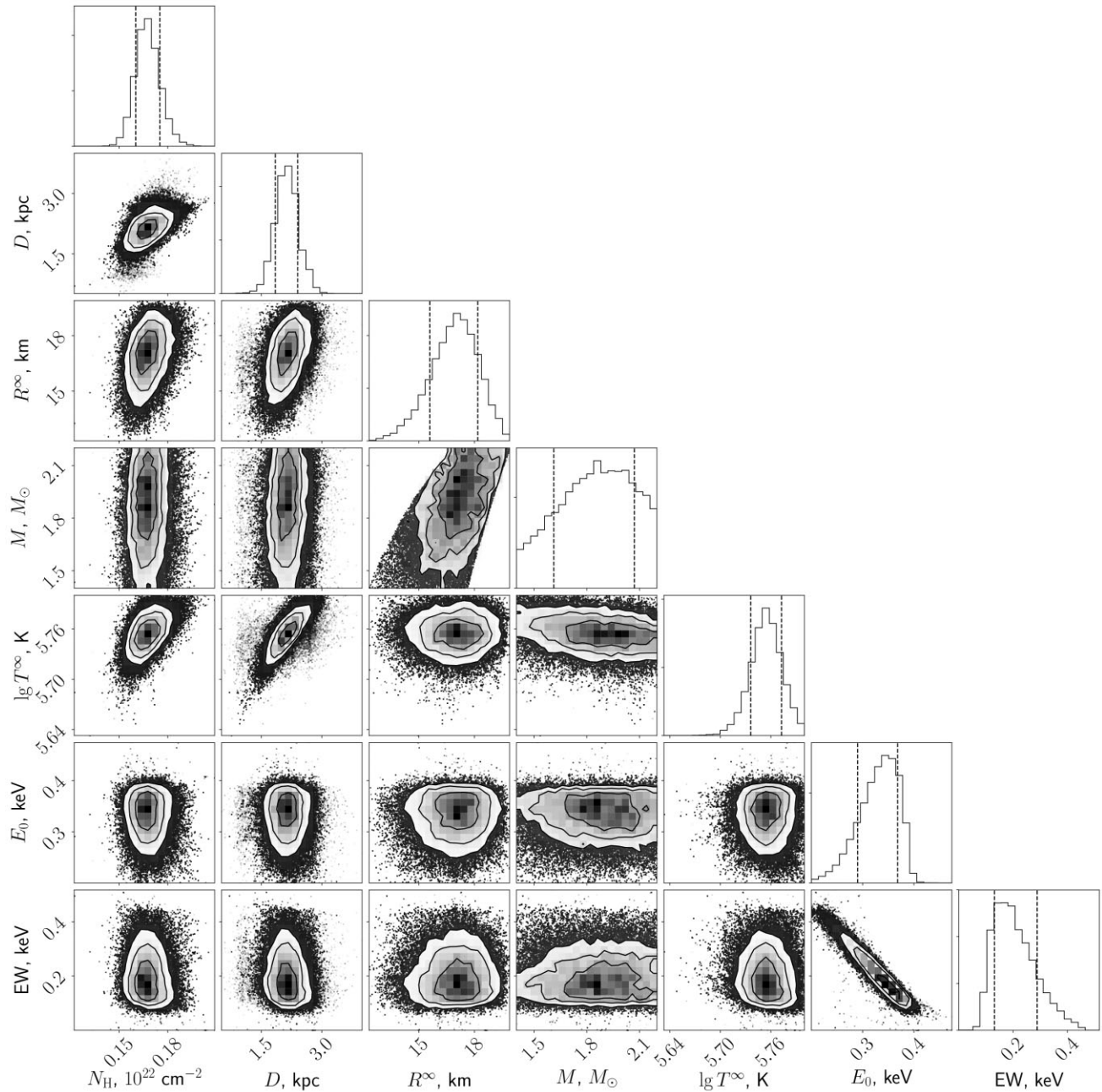**Figure 8.** 1D and 2D marginal posterior distribution functions for some parameters of the (NS133 + PL) × GABS model. Contours in 2D distributions correspond to 39 per cent, 68 per cent, and 86 per cent confidence levels. In 1D distributions, vertical dashed lines indicate 1σ credible intervals.

or $\approx(3\text{--}4) \times 10^{13}$ G if it is produced by heavier ions. The first value is $\sim$200 times lower and the second is about an order of magnitude higher than the estimated spin-down magnetic field (see Table 1 and Appendix B). Thus, the electron cyclotron line can be created at a few stellar radii above the NS surface, e.g. in a radiation belt, where the magnetic field is much weaker (see e.g. Luo & Melrose 2007). Otherwise, if it is an ion cyclotron line, then the magnetic field at the surface is considerably stronger than the B values estimated in Appendix B and used in our atmosphere modelling. Such a cyclotron line might indicate the presence of strong multipole field components (cf. Bilous et al. 2019; Lockhart et al. 2019) or magnetic loops (Tiengo et al. 2013; Mereghetti, Pons & Melatos 2015; Rodríguez Castillo et al. 2016), which are not considered in our models. We also

note that magnetized atmosphere models predict too low EW of the proton cyclotron line in comparison with the observed one (cf. the discussion of a similar case by Hambaryan et al. 2017). In particular, our dipolar models show that the proton cyclotron line is damped by the smearing due to magnetic field variations over the surface (see Fig. B1).

Alternatively, the feature may be formed by atomic transitions in a non-hydrogen atmosphere (e.g. Mori & Ho 2007), the ISM, or a cloud near the outer part of the magnetosphere (cf. Hambaryan et al. 2009; Pires et al. 2019).

Finally, we cannot exclude the possibility that the absorption feature is an instrumental artefact. The addition of the line improves significantly the fit of the PN spectrum but does not influence the

statistics for the MOS data. However, this is not surprising since the former spectrum contains much more counts. To check whether it is the artefact, it would be useful to examine whether the spectra of other sources in the PN FoV show similar features. Unfortunately, all other sources are not bright enough to perform such analysis. Phase-resolved spectral analysis of J0554 could also help to clarify the nature of the feature in its emission. However, this is impossible because of the low count statistics.

The non-thermal X-ray luminosity of J0554 in the 2–10 keV band $L_X \approx (1.6–1.9) \times 10^{30}$ erg s^{-1} for the (NSMDINTB + PL) × GABS models and 1.2×10^{31} erg s^{-1} for the (2BB+PL) × GABS model. The corresponding X-ray efficiencies $\eta_X = L_X/\dot{E} \approx 10^{-4.8}–10^{-4.9}$ and $10^{-3.7}$, respectively.[9] For a 52-kyr-old pulsar these values are compatible with the dependencies $L_X(t_c)$ and $\eta_X(t_c)$ based on observations of other X-ray emitting pulsars (see e.g. Zharikov & Mignani 2013).

Using the N_H–D relation, we found the distance to J0554 to be 1.6–2.4 kpc in the case of the atmosphere models. This is compatible with the 'pseudo-distance' of 1.9 kpc based on the γ-ray data. If this estimate is correct, the SNR G179.0+2.6 is located somewhat closer than relations between the radio surface brightness and the diameter of the SNR predict. On the other hand, the (2BB+PL) × GABS model resulted in the larger distance of 2.7–5.5 kpc. This agrees with the upper limit on the distance to G179.0+2.6 of about 5 kpc provided by How et al. (2018).

We detected, for the first time, X-ray pulsations with the J0554 spin period. The pulse profile shows two peaks per period. The pulsed fraction in the 0.2–2 keV band is 25 ± 6 per cent. This is a typical value for the thermal emission originated from the bulk of an NS surface (e.g. Pavlov & Zavlin 2000a). Using the pulse profile, we can set additional constraints on the angles α and ζ in the case of the atmosphere models. The J0554 observed and theoretical light curves are shown in Fig. 9. The maximum PF provided by the models NSMDINTB in the 0.2–2 keV band is ≈ 20 per cent. This is somewhat lower than the measured value but is compatible with it within uncertainties. The corresponding α and ζ both lie in the range of 50°–70° that is compatible with the results of the spectral analysis (Table 2). Despite the low number of counts, there is a marginal peak in the 2–4 keV pulse profile that coincides with the smaller peak in the 0.2–2 keV band (see Fig. 5). This may indicate the pulsations of the non-thermal component. As can be seen from Fig. 7, its flux in the 0.2–2 keV band is significantly lower than that of the thermal component. Nevertheless, it may contribute to the pulsed flux and thus somewhat increase the model predicted PF. It may also be responsible for some asymmetry of the pulse profile. The inset in Fig. 9 shows the 90 per cent confidence contours of the 2D distribution of the angles α and ζ at fixed values of M, R, B, and T^∞. These contours are obtained assuming that the flux values, derived from the number of counts in the 9 phase bins, are normally distributed and uncorrelated.

In contrast to the atmosphere models, the light curves for the 2BB model are almost flat. This is because the BB components assume uniform temperature distribution over the emitting areas and isotropic radiation (unlike the peaked radiation from the magnetized atmospheres), but mainly because of the smallness of the ratio of the fluxes from the hot and cold BB components. Taking the most
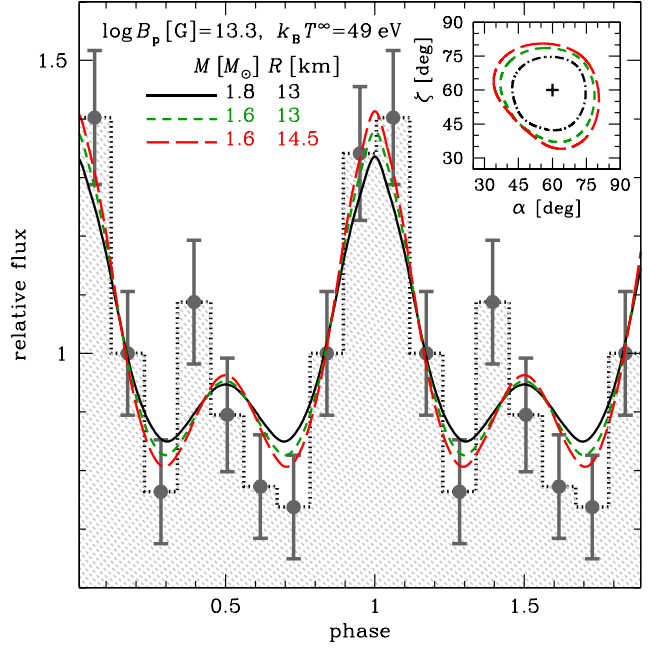

Figure 9. J0554 pulse profile in the 0.2–2 keV band (grey dotted histogram with error bars) and theoretical light curves computed for the model NS133 with $\alpha = \zeta = 60°$, $k_BT = 49$ eV, and for three different combinations of the mass M and radius R of the NS, drawn using different line styles as specified in the legend, which cover the range of pulsed fractions from ≈ 15 per cent (black solid line) to ≈ 19.5 per cent (red dashed line). The inset shows the contours at the 90 per cent confidence level on the (α, ζ) plane for the same three NS models.

probable values for the model (2BB+PL) × GABS from Table 2, we obtained the strict upper limit PF < 3.2 per cent, which is incompatible with the observed one.

6.2 J0554 and NS cooling theories

The comparison of the measured thermal luminosity with predictions of NS cooling theories can provide constraints on the EoS and other properties of the NS matter and tests for theoretical models of such matter. In Fig. 10, we demonstrate examples of such comparison. Here, the cooling curves, which show the time dependence of the bolometric thermal luminosity of the star in the reference frame of a distant observer, $L^\infty(t^\infty)$, have been produced using the computer code presented by Potekhin & Chabrier (2018) with essentially the same microphysics input. The most uncertain microphysics ingredients that can significantly affect the cooling are the EoS and composition of the NS core, composition of the heat-blanketing outer envelopes, and density dependences of the critical temperatures of the baryon superfluidity in the core (see e.g. Potekhin, Pons & Page 2015, for review). Here we show the cooling curves for two EoSs and for two models of the heat-blanketing envelopes composition. For the EoS and composition of the core we employ two widely used models: the model BSk24 (Pearson et al. 2018) and the model A18+δv+UIX* (Akmal, Pandharipande & Ravenhall 1998), which is hereafter named APR* and parametrized according to Potekhin & Chabrier (2018). Both EoSs describe the $npe\mu$ matter, which consists of the leptons and nucleons without allowance for other baryons or free quarks. For the composition of the non-accreted crust and envelopes, we use the BSk24 model of the ground-state matter. The alternative model is the accreted envelope with helium filling the heat-blanketing
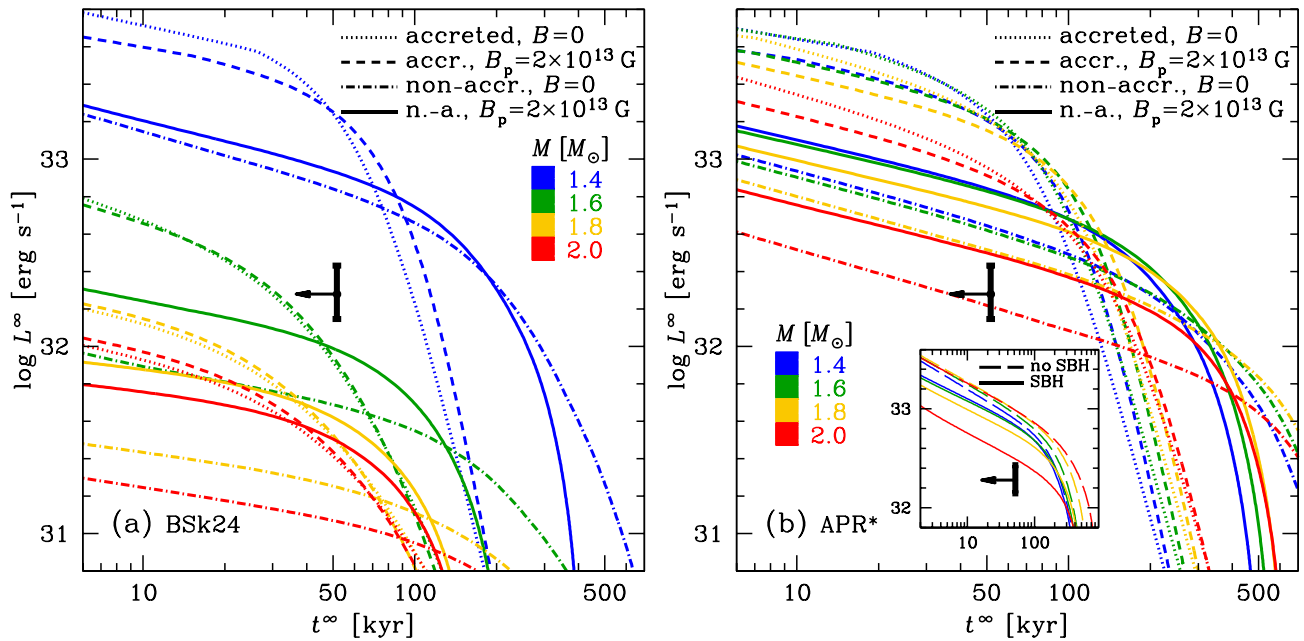
---

[9]For the (NSMDINTB + PL) × GABS models, we recalculated the spin-down luminosity using the best-fitting parameters and the formula for the moment of inertia by Ravenhall & Pethick (1994). The resulting $\dot{E} = (1.2–1.4) \times 10^{35}$ erg s^{-1}. For the (2BB+PL) × GABS model, we used $\dot{E}$ from Table 1.

Figure 10. Theoretical cooling curves, calculated according to the EoS models BSk24 (panel a) and APR* (panel b), compared with observational estimates of the thermal luminosity and age of J0554 (the error bar). The cooling curves for NS models with masses $M = 1.4$, 1.6, 1.8, and 2.0 $M_\odot$ (coded by colour), endowed with a dipole magnetic field having the strength $B_{\rm p} = 2 \times 10^{13}$ G at the pole, are shown by solid and dashed lines, respectively, for non-accreted and accreted heat blanketing envelopes (see text for details). For comparison, cooling curves for analogous non-magnetic NS models are shown, respectively, by dot–dashed and dotted lines. The inset to panel (b) illustrates the role of the enhancement of the modified Urca processes described by Shternin, Baldo & Haensel (2018, SBH). Here, the solid and long-dashed cooling curves are computed, respectively, with and without taking the SBH effect into account.

layers up to the density $\rho = 10^9$ g cm^{-3} (cf. Beznogov, Potekhin & Yakovlev 2021) and with the ground-state composition at higher densities. We use the model of a magnetized envelope with the surface distribution of magnetic field and local effective temperature consistent with the atmosphere model described in Appendix B, with the polar magnetic strength $B_{\rm p} = 2 \times 10^{13}$ G. We assume that the field is a relativistic dipole not only in the atmosphere but also in the stellar core. Accordingly, we take into account the effects of Landau quantization on the EoS and thermal conductivities in the outer crust and envelopes and the heat loss due to the synchrotron and fluxoid-scattering mechanisms of neutrino emission, as well as magnetically induced modifications of other neutrino emission mechanisms (see Potekhin, Pons & Page 2015 and references therein). For comparison, for each EoS and each envelope composition, we also plot a cooling curve for the same NS without magnetic field.

The baryon superfluidity in the $npe\mu$ matter of an NS can be of three types, characterized by the neutron singlet or triplet and proton singlet pairing. The theory of the neutron singlet superfluidity, which occurs in the inner crust of an NS, is sufficiently robust (see Ding et al. 2016); specifically, here we use the MSH model (Margueron, Sagawa & Hagino 2008) in the parametrized form by Ho et al. (2015). In contrast, there are several substantially different theoretical models for the other two types of superfluidity that operate in the NS core and considerably affect the cooling (see e.g. Page et al. 2014; Sedrakian & Clark 2019, for review). For illustration, we use the parametrizations from Ho et al. (2015) for the BS (Baldo & Schulze 2007) and TTav (Takatsuka & Tamagaki 2004) models of the proton singlet and neutron triplet superfluidity types, respectively.

The error bar in Fig. 10 embraces the 1σ limits to the measured thermal luminosity L^∞ for the atmosphere models (the last two columns of Table 2). It is placed at $t^\infty = t_{\rm c}$, and the leftward

arrow indicates that the true age of the pulsar is likely somewhat smaller. This expectation is based on the fact that usually (although not always) true ages of pulsars are smaller than their characteristic ages (see e.g. Potekhin et al. 2020).

Fig. 10(a) shows the cooling curves for the BSk24 model. These cooling curves pass above the observational error bar for the NS model with $M = 1.4$ $M_\odot$, but below it for the models with $M \geq 1.6$ $M_\odot$. The fast cooling of the massive NSs is mainly due to the powerful direct Urca processes of neutrino emission, which operate at sufficiently high densities in the cores of these stars and overpower the more common modified Urca processes. This cooling enhancement occurs if M exceeds a certain threshold value (e.g. Haensel 1995), which is slightly below 1.6 $M_\odot$ for the BSk24 model (Pearson et al. 2018). The observations can be made compatible with the enhanced cooling models, if we assume that the true age of J0554 is smaller than $t_{\rm c}$. Among the cooling curves shown in Fig. 10(a), the smallest discrepancy between the true and characteristic ages is required for the NS with $M = 1.6$ $M_\odot$ and accreted envelope. In this case M is only slightly larger than $M_{\rm DU}$, so that the direct Urca processes operate only in a small central part of the NS core.

Fig. 10(b) shows the cooling curves for the APR* model. For this EoS, the direct Urca processes cannot occur for $M \lesssim 2\,{\rm M}_\odot$. However, the non-enhanced (so-called minimal) cooling can be compatible with the observations of J0554 in this case, if the blanketing envelope is non-accreted. It is worthwhile to note that the latter compatibility is achieved due to the enhancement of the modified Urca processes, recently discovered by Shternin et al. (2018). This enhancement becomes very strong near the threshold density for opening the direct Urca process. For the APR* model, the threshold mass only slightly exceeds 2 $M_\odot$, therefore the effect of Shternin et al. (2018) significantly enhances the total neutrino luminosity of the NS with

$M = 2\,M_\odot$ and thus decreases its temperature. In the absence of such enhancement, the luminosity would be higher for NS models with higher masses in the minimal cooling scenario, as illustrated by the long-dashed curves in the inset to Fig. 10(b), because more massive stars have larger heat capacities.

The presented analysis is self-consistent in the sense that cooling scenarios for BSk24 and APR* models are considered taking into account the NS parameters (mass, radius, and magnetic field) obtained from the spectral fit. In order to give preference to one of the EoSs, better constraints on the NS mass and true age are required.

7 SUMMARY

Using 45-ks *XMM–Newton* observations we detected a soft point-like X-ray source within 1σ area of the *Fermi* position of the γ-ray pulsar J0554+3107, confirming the earlier *Swift* detection at much higher significance. We firmly established the pulsar nature of the source by detecting coherent pulsations with the J0554 frequency in the 0.2–2 keV band. The pulse profile demonstrates two peaks separated by about a half of the rotation phase. The background-corrected pulsed fraction is 25 ± 6 per cent. Marginal single-peaked pulsations are seen in the hard band above 2 keV, but low number of counts precludes definite conclusions.

The spectral analysis shows that the thermal emission from the surface of the NS dominates at energies below ≈ 2 keV, while a weak non-thermal magnetospheric component may be present in the hard band. To describe the former, we constructed a set of the NS hydrogen atmosphere models with dipole magnetic field. In order to fit the data they require addition of the absorption line at ≈ 0.35 keV. The nature of the feature is unclear. Among the possibilities are cyclotron absorption, atomic transitions in the ISM or NS atmosphere, or an instrumental artefact. Implementing the absorption column density–distance relation, we estimated the distance to the pulsar to be ≈ 2 kpc. We note that the combination of two blackbody components, corresponding to the cold NS surface with a hotspot on it, and the absorption line also provides statistically acceptable fit, resulting in about twice as large distance. However, this model is less physically realistic and it fails to reproduce the observed pulse profile with the pulsed fraction $\gtrsim 20$ per cent. Therefore, we consider the atmosphere models as more appropriate ones.

The best-fitting parameters obtained for the atmosphere models suggest that J0554 is a rather heavy NS with the mass in the range of 1.6–2.1 $M_\odot$ and the radius of about 13 km. The redshifted effective temperature of ≈ 50 eV corresponds to the bolometric luminosity of $\approx 2 \times 10^{32}$ erg s^{-1} as seen by a distant observer. Utilising this value, together with the pulsar characteristic age of 50 kyr, we investigated cooling scenarios for J0554 in the frame of two popular EoSs. For the BSk24 model, the observed bolometric luminosity is consistent with the predictions if the mass of the NS is close to the lower limit of the range obtained from the spectral fit, and if the true age of J0554 is substantially smaller than the characteristic one. This model also favours the presence of the accreted heat-blanketing envelope. On the other hand, the APR* model requires non-accreted envelope and the mass close to 2.0 $M_\odot$, which leads to effective cooling of the NS through modified Urca processes and compatibility of the model cooling curve with observations if the true age of J0554 is close to the characteristic one.

Deeper X-ray observations are necessary to better constrain the J0554 parameters. Phase-resolved spectral analysis would allow one to unveil the nature of the absorption feature and to better constrain the pulsar geometry. Measurement of the pulsar proper motion could confirm the association of J0554 and SNR G179.0+2.6 and provide an independent estimate of their age.

DATA AVAILABILITY

The *XMM–Newton* data are available through the data archive https://www.cosmos.esa.int/web/xmm-newton/xsa.

REFERENCES

Akmal A., Pandharipande V. R., Ravenhall D. G., 1998, Phys. Rev. C, 58, 1804

Arnaud K. A., 1996, in Jacoby G. H., Barnes J., eds, ASP Conf. Ser. Vol. 101, Astronomical Data Analysis Software and Systems V. Astron. Soc. Pac., San Francisco, p. 17

Arumugasamy P., Kargaltsev O., Posselt B., Pavlov G. G., Hare J., 2018, ApJ, 869, 97

Baldo M., Schulze H. J., 2007, Phys. Rev. C, 75, 025802

Becker W., Trümper J., 1999, A&A, 341, 803

Bejger M., Haensel P., 2002, A&A, 396, 917

Beznogov M. V., Potekhin A. Y., Yakovlev D. G., 2021, Phys. Rep., 919, 1

Bilous A. V. et al., 2019, ApJ, 887, L23

Buccheri R. et al., 1983, A&A, 128, 245

Capitanio L., Lallement R., Vergely J. L., Elyajouri M., Monreal-Ibero A., 2017, A&A, 606, A65

Case G. L., Bhattacharya D., 1998, ApJ, 504, 761

Chen B. Q. et al., 2014, MNRAS, 443, 1192

Chen B. Q. et al., 2019, MNRAS, 483, 4277

Deutsch A. J., 1955, Ann. d'Astrophys., 18, 1

Ding D., Rios A., Dussan H., Dickhoff W. H., Witte S. J., Carbone A., Polls A., 2016, Phys. Rev. C, 94, 025802

Drimmel R., Cabrera-Lavers A., López-Corredoira M., 2003, A&A, 409, 205

Evans P. A. et al., 2014, ApJS, 210, 8

Foight D. R., Güver T., Özel F., Slane P. O., 2016, ApJ, 826, 66

Foreman-Mackey D., Hogg D. W., Lang D., Goodman J., 2013, PASP, 125, 306

Fuerst E., Reich W., 1986, A&A, 154, 303

Gao X. Y., Han J. L., Reich W., Reich P., Sun X. H., Xiao L., 2011, A&A, 529, A159

Ginzburg V. L., Ozernoy L. M., 1965, Sov. Phys. JETP, 20, 689

Goodman J., Weare J., 2010, Commun. Appl. Math. Comput. Sci., 5, 65

Green G. M., Schlafly E., Zucker C., Speagle J. S., Finkbeiner D., 2019, ApJ, 887, 93

Grießmeier J. M., Smith D. A., Theureau G., Johnson T. J., Kerr M., Bondonneau L., Cognard I., Serylak M., 2021, A&A, 654, A43

Guseinov O. H., Ankay A., Sezer A., Tagieva S. O., 2003, Astron. Astrophys. Trans., 22, 273

Haensel P., 1995, Space Sci. Rev., 74, 427

Hambaryan V., Neuhäuser R., Haberl F., Hohle M. M., Schwope A. D., 2009, A&A, 497, L9

Hambaryan V., Suleimanov V., Haberl F., Schwope A. D., Neuhäuser R., Hohle M., Werner K., 2017, A&A, 601, A108

Ho W. C. G., Elshamouty K. G., Heinke C. O., Potekhin A. Y., 2015, Phys. Rev. C, 91, 015806

How T. G., Fesen R. A., Neustadt J. M. M., Black C. S., Outters N., 2018, MNRAS, 478, 1987

Kargaltsev O., Pavlov G. G., 2008, in Bassa C., Wang Z., Cumming A., Kaspi V. M., eds, AIP Conf. Proc. Vol. 983, 40 Years of Pulsars: Millisecond Pulsars, Magnetars and More. Am. Inst. Phys., New York, p. 171

Kargaltsev O., Durant M., Misanovic Z., Pavlov G. G., 2012, Science, 337, 946

Lallement R., Vergely J. L., Valette B., Puspitarini L., Eyer L., Casagrande L., 2014, A&A, 561, A91

Lallement R. et al., 2018, A&A, 616, A132

Lockhart W., Gralla S. E., Özel F., Psaltis D., 2019, MNRAS, 490, 1774

Lower M. E. et al., 2021, MNRAS, 508, 3251

Luo Q., Melrose D., 2007, MNRAS, 378, 1481

McLaughlin M. A. et al., 2007, ApJ, 670, 1307

Manchester R. N., Hobbs G. B., Teoh A., Hobbs M., 2005, AJ, 129, 1993

Margueron J., Sagawa H., Hagino K., 2008, Phys. Rev. C, 77, 054309

Mereghetti S., Pons J. A., Melatos A., 2015, Space Sci. Rev., 191, 315

Mereghetti S., Rigoselli M., Taverna R., Baldeschi L., Crestan S., Turolla R., Zane S., 2021, ApJ, 922, 253

Miller J. J., McLaughlin M. A., Rea N., Lazaridis K., Keane E. F., Kramer M., Lyne A., 2013, ApJ, 776, 104

Mori K., Ho W. C. G., 2007, MNRAS, 377, 905

Page D., Lattimer J. M., Prakash M., Steiner A. W., 2014, in Bennemann K.-H., Ketterson J. B., eds, Novel Superfluids, Vol. 2. Oxford Univ. Press, Oxford, p. 505

Pavlov G. G., Zavlin V. E., 2000a, in Martens P. C. H., Tsuruta S., Weber M. A., eds, Proc. IAU Symp. 195, Highly Energetic Physical Processes and Mechanisms for Emission from Astrophysical Plasmas. Astron. Soc. Pac., San Francisco, p. 103

Pavlov G. G., Zavlin V. E., 2000b, ApJ, 529, 1011

Pavlovic M. Z., Dobardzic A., Vukotic B., Urosevic D., 2014, Serbian Astron. J., 189, 25

Pearson J. M., Chamel N., Potekhin A. Y., Fantina A. F., Ducoin C., Dutta A. K., Goriely S., 2018, MNRAS, 481, 2994

Pétri J., 2019, MNRAS, 485, 4573

Pires A. M., Schwope A. D., Haberl F., Zavlin V. E., Motch C., Zane S., 2019, A&A, 623, A73

Pletsch H. J. et al., 2013, ApJ, 779, L11

Potekhin A. Y., 2014, Phys. Uspekhi, 57, 735

Potekhin A. Y., Chabrier G., 2003, ApJ, 585, 955

Potekhin A. Y., Chabrier G., 2018, A&A, 609, A74

Potekhin A. Y., Yakovlev D. G., Chabrier G., Gnedin O. Y., 2003, ApJ, 594, 404

Potekhin A. Y., Lai D., Chabrier G., Ho W. C. G., 2004, ApJ, 612, 1034

Potekhin A. Y., Chabrier G., Ho W. C. G., 2014, A&A, 572, A69

Potekhin A. Y., Pons J. A., Page D., 2015, Space Sci. Rev., 191, 239

Potekhin A. Y., Zyuzin D. A., Yakovlev D. G., Beznogov M. V., Shibanov Y. A., 2020, MNRAS, 496, 5052

Ravenhall D. G., Pethick C. J., 1994, ApJ, 424, 846

Rigoselli M., Mereghetti S., Suleimanov V., Potekhin A. Y., Turolla R., Taverna R., Pintore F., 2019, A&A, 627, A69

Rodríguez Castillo G. A. et al., 2016, MNRAS, 456, 4145

Sale S. E. et al., 2014, MNRAS, 443, 2907

Saz Parkinson P. M. et al., 2010, ApJ, 725, 571

Schwope A. et al., 2022, A&A, 661, A41

Sedrakian A., Clark J. W., 2019, Eur. Phys. J. A, 55, 167

Shevchuk A. S. H., Fox D. B., Rutledge R. E., 2009, ApJ, 705, 391

Shibanov Y., Danilenko A., Zharikov S., Shternin P., Zyuzin D., 2016, ApJ, 831, 112

Shternin P. S., Baldo M., Haensel P., 2018, Phys. Lett. B, 786, 28

Spitkovsky A., 2006, ApJ, 648, L51

Sturrock P. A., 1971, ApJ, 164, 529

Suleimanov V., Potekhin A. Y., Werner K., 2009, A&A, 500, 891

Swanepoel J. W. H., de Beer C. F., Loots H., 1996, ApJ, 467, 261

Takatsuka T., Tamagaki R., 2004, Progress Theor. Phys., 112, 37

Tiengo A. et al., 2013, Nature, 500, 312

Tyul'bashev S. A., Kitaeva M. A., Tyulbasheva G. E., 2021, Astron. Rep., 65, 819

Wachter K., Leach R., Kellogg E., 1979, ApJ, 230, 274

Willatt R., Ehle M., 2016, Guide for Use of the Images Script. https://www.cosmos.esa.int/documents/332006/641121/README.pdf

Wilms J., Allen A., McCray R., 2000, ApJ, 542, 914

Yakovlev D. G., Pethick C. J., 2004, ARA&A, 42, 169

Zhao H., Jiang B., Li J., Chen B., Yu B., Wang Y., 2020, ApJ, 891, 137

Zharikov S., Mignani R. P., 2013, MNRAS, 435, 2227

Zharikov S., Zyuzin D., Shibanov Y., Kirichenko A., Mennickent R. E., Geier S., Cabrera-Lavers A., 2021, MNRAS, 502, 2005

Zyuzin D. A., Karpova A. V., Shibanov Y. A., 2018, MNRAS, 476, 2177

Zyuzin D. A., Karpova A. V., Shibanov Y. A., Potekhin A. Y., Suleimanov V. F., 2021, MNRAS, 501, 4998

APPENDIX A: PULSATIONS DETECTION SIGNIFICANCE AND SPIN FREQUENCY UNCERTAINTY

To estimate the confidence level of the detection of the periodic signal from J0554, we generated 1 million synthetic light curves with the length and the mean count rate equal to the ones observed from J0554, but consisting of pure Poisson noise without any periodic component. For each of the light curves, we performed Z_2^2-test using the same frequency window and the same number of trial frequencies as for Z_2^2-test on the observed light curve. The obtained highest Z_2^2 values were used to construct the cumulative distribution function (CDF) of Z_2^2 in the absence of the periodic signal (see Fig. A1). We found that the probability to get $Z_2^2 = 42.7$ from pure noise is about 2×10^{-6}, which corresponds to the detection confidence level of $\approx 4.7\sigma$.

The frequency uncertainty was estimated in a similar fashion. We fitted the pulse profile with the sum of the first two harmonics. We simulated 1000 event lists of the periodic signal with the measured frequency, amplitudes and relative phases of two harmonics, keeping the mean count rate fixed, and varying the number of photons and their times of arrival according to the Poisson statistics. For each event list, we found the frequency of the signal performing Z_2^2-test identical to the one applied to the real data. The nearly symmetrical 68 per cent confidence interval of the resulting frequency distribution (see Fig. A2) was taken as the desired uncertainty.
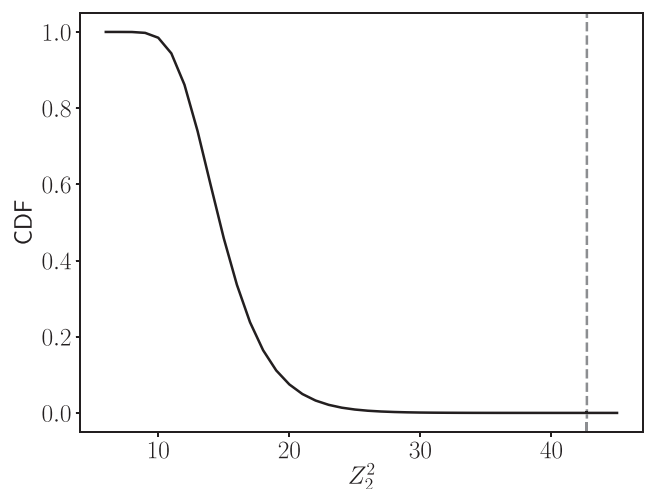

Figure A1. Cumulative distribution function of Z_2^2 for a pure noise signal with the mean count rate equal to the observed from J0554. The vertical dashed line corresponds to $Z_2^2 = 42.7$.
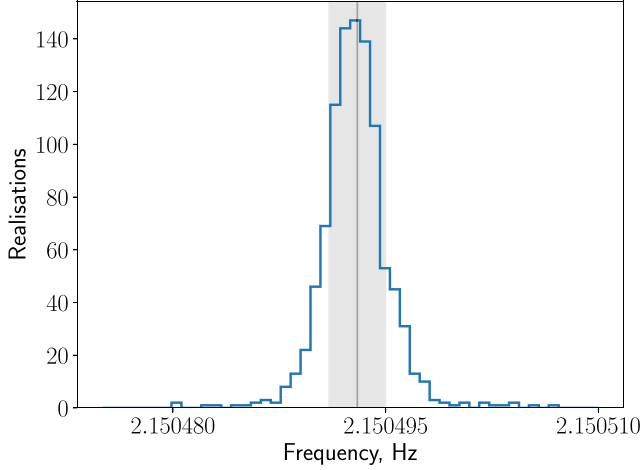
Figure A2. Distribution of the best frequencies measured for 1000 simulated event lists with the parameters fixed at the values obtained for J0554. The solid vertical line corresponds to the most probable value, while the shaded area indicates the 68 per cent credible interval that was taken as the error of the frequency determination.

APPENDIX B: ATMOSPHERE MODELS

The computation of the spectrum that can be measured by a distant observer is patterned after Zyuzin et al. (2021). We construct the integral spectrum by assembling local spectra at different patches on the surface. We assume a dipolar magnetic field, modified by the effects of general relativity (Ginzburg & Ozernoy 1965; Pavlov & Zavlin 2000b). The temperature distribution, which is associated with this magnetic field, is calculated following Potekhin et al. (2003).

For every selected field strength at the magnetic pole B_p and selected NS mass and radius, the local radiative flux density was computed at three magnetic latitudes, including the pole, for a set of 480 directions of the photon wave vector and for 150–200 photon energies in the X-ray band, using an advanced version of the code described in Suleimanov, Potekhin & Werner (2009). The fourth latitude is the equator, which is too cold to allow construction of an atmosphere model with the currently available opacities in strong magnetic fields for the selected range of effective temperatures $\log T^{\infty}$ (K) = 5.4–5.8. However, its contribution to the total flux is small, so we replace it by the blackbody model (we have checked that using alternative models does not lead to a noticeable change in the total spectrum).

The code of Suleimanov et al. (2009) has been modified to allow for different angles θ_B between the magnetic field and the normal to the surface. Hydrogen composition is considered, taking into account incomplete ionization. The effects of the strong magnetic field and the atomic thermal motion across the field on the plasma opacities are treated following Potekhin & Chabrier (2003) with the improvements described in Potekhin, Chabrier & Ho (2014). Polarization vectors and opacities of normal electromagnetic modes are calculated as in Potekhin et al. (2004). Then flux values at arbitrary latitudes, energies, and directions are obtained by interpolation (or extrapolation, whenever needed).

The monochromatic spectral flux density measured by a distant observer is computed by integrating the emission from different local patches over the stellar surface for any selected angle Θ_m between the magnetic dipole axis and the line of sight (see appendix A of Zyuzin et al. 2021 for details). In the axisymmetric model, the pulsar geometry is determined by the angles α and ζ that the spin axis
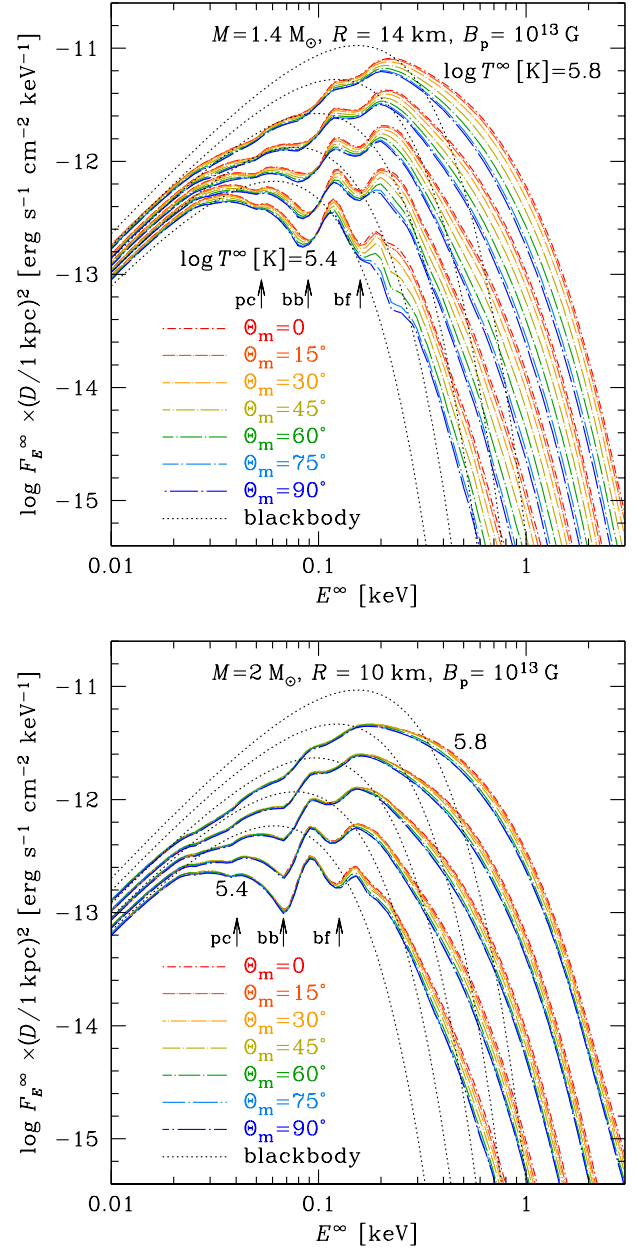

Figure B1. Top panel: thermal spectra of an NS model with $M = 1.4\,M_{\odot}$, $R = 14$ km, and $B_p = 10^{13}$ G, as seen by a distant observer, for $\log T^{\infty}_{\text{eff}}$ (K) = 5.4, 5.5, 5.6, 5.7, and 5.8 (the five bunches of lines from bottom to top), and seven values of the angle between the magnetic axis and the line of sight, Θ_m (different line styles and colours according to the legend). The arrows indicate approximate positions of the features due to the proton cyclotron absorption (pc), the principal bound–bound transition (bb), and the principal photoionization threshold (bf), smeared by the field distribution over the surface and/or by atomic motion effects. For comparison, the dotted lines show the blackbody spectra for the same NS parameters and redshifted effective temperatures T^{∞}. Bottom panel: the same as in the top panel but for an NS model with $M = 2\,M_{\odot}$ and $R = 10$ km.

makes with the magnetic axis and with the line of sight, respectively (e.g. Pavlov & Zavlin 2000b). To produce phase-resolved spectra, it is sufficient to calculate $\cos \Theta_m = \sin \zeta \sin \alpha \cos \phi + \cos \alpha \cos \zeta$ for each rotation phase ϕ. Then the light curve and the phase-integrated

spectrum are given by integration of the phase-resolved spectrum over the energy or over the phase ϕ, respectively.

For isolated pulsars, the widely used estimate of the magnetic field strength is based on the expression

$$B \approx 3.2 \times 10^{19} C \sqrt{P \dot{P}} \, \text{G}, \tag{B1}$$

where P is the period in seconds, $\dot{P}$ is the period time derivative, and C is a coefficient, which depends on stellar parameters. For the non-relativistic rotating magnetic dipole in vacuo (Deutsch 1955), the magnetic field strength at the equator B_{eq} is given by setting

$$C = R_{10}^{-3} (\sin \alpha)^{-1} \sqrt{I_{45}}, \tag{B2}$$

where $R_{10} \equiv R/(10 \text{ km})$ and I_{45} is the moment of inertia in units of 10^{45} g cm^2. The latter depends on the EoS, but in most plausible settings it can be estimated with an accuracy within 10 per cent by the approximation of Ravenhall & Pethick (1994), which can be written in the form

$$I_{45} \approx 0.42(M/M_{\odot})(R^{\infty}/10 \text{ km})^2 \tag{B3}$$

(see Bejger & Haensel 2002 for a more general fitting formula). The characteristic field B_c (Table 1) is defined by equation (B1) with $C = 1$ (e.g. Manchester et al. 2005). For the likely values of $\alpha \gtrsim 50°$, $M \approx (1.6–2.1)$ M$_{\odot}$, and $R \approx 11.7–14.7$ km, implied by the fitting results in Table 2, equations (B1)–(B3) give $B_{eq} \sim (4–11) \times 10^{12}$ G, which implies, for the non-relativistic dipole field, $B_p \sim (0.8–2.2) \times 10^{13}$ G.

These values are consistent with the values $B_p = 10^{13}$ and 2×10^{13} G that we used to construct the atmosphere models. We have also tried models with lower and higher field strengths, but found that they do not provide a better fit.

A real pulsar differs from a rotating magnetic dipole, because its magnetosphere is filled with plasma, carrying electric charges and currents. According to the results of numerical simulations of plasma behaviour in the pulsar magnetosphere (Spitkovsky 2006), the equatorial magnetic field can be approximately described by equation (B1) with

$$C \approx (0.8 \pm 0.1)R_{10}^{-3}(1 + \sin^2 \alpha)^{-1/2} \sqrt{I_{45}}, \tag{B4}$$

which gives estimates in the range of $B_p \sim (3–9) \times 10^{12}$ G. Additional uncertainties arise from the effects of general relativity, pulsar wind, and deviations from the pure dipole geometry (see Pétri 2019 for discussion and references).

For each of the selected B_p values, we have considered M, R, T^{∞}, α, and ζ as fitting parameters, using interpolation and extrapolation based on the computed spectra for $M = 1.4$ and 2.0 M$_{\odot}$, $R = 10$, 12, and 14 km, log T^{∞} (K) = 5.4, 5.5, 5.6, 5.7, and 5.8, and various Θ_m. Examples of the computed spectra are shown in the top and bottom panels of Fig. B1 for less and more compact NS models, respectively.

This paper has been typeset from a TEX/LATEX file prepared by the author.